



# OPEN Au-H<sub>2</sub>Ti<sub>3</sub>O<sub>7</sub> nanotubes for non-invasive anticancer treatment by simultaneous photothermal and photodynamic therapy

Maher I. Al-Shemri<sup>1</sup>, Maryam Aliannezhadi<sup>1</sup>✉, Rana A. Ghaleb<sup>2</sup> & Mohammed J. Al-Awady<sup>3</sup>

Treating lung and prostate cancer cells is a major health problem that may be solved through the interactions of laser beams with nanoparticles. In the paper, Au-H<sub>2</sub>Ti<sub>3</sub>O<sub>7</sub> nanotubes (NTs) are proposed as a treatment agent and the interactions of different laser beams with the nanostructure are considered to solve the mentioned health problem. Also, the NTs are employed to treat the cancers in dark conditions. The results are motivating because Au-H<sub>2</sub>Ti<sub>3</sub>O<sub>7</sub> NPs do not affect healthy cells, while they strongly affect cancer cells, and the viability percentage of LNCap cells reaches 16% for incubation times of 48 h. Furthermore, treating LNCap cells using the irradiated Au-H<sub>2</sub>Ti<sub>3</sub>O<sub>7</sub> NTs by NIR beam at 808 nm has no cytotoxicity, while cytotoxicity of 92% is obtained using an irradiation laser beam at 532 nm. Also, applying the laser beam at 635 nm to the NTs leads to a cytotoxicity of ~53% in lung cancer (A549 cells). In total, the Au-H<sub>2</sub>Ti<sub>3</sub>O<sub>7</sub> NTs have a selective effect on cancer cells and greatly reduce the viability in the given dark and irradiation conditions, leading to the introduction of them as a promising agent for the non-invasive treatment of prostate cancer and a moderate candidate for lung cancer therapy.

**Keywords** H<sub>2</sub>Ti<sub>3</sub>O<sub>7</sub> nanotubes, Plasmonic nanoparticles, Interactions of laser beams with nanostructures, Lung and prostate cancer, Photothermal and photodynamic therapy

Photodynamic therapy (PDT) is an innovative medical treatment that integrates the use of light with a photosensitizing agent to selectively target and destroy cancer cells or other abnormal tissues. The process entails the administration of a photosensitizer, which selectively accumulates in the target area. Upon activation by specific wavelengths of light, the photosensitizer generates reactive oxygen species, leading to cellular damage and subsequent destruction of the target tissue<sup>1,2</sup>. PDT has gained significant attention due to its minimally invasive nature and potential for localized treatment. It has shown promising results in various cancer types, such as skin, lung, and esophageal cancers, as well as in treating certain non-cancerous conditions. This therapeutic approach offers several advantages, including reduced side effects and the ability to repeat treatments. PDT continues to evolve as a valuable treatment modality, offering a unique option in the oncology field<sup>2-5</sup>.

Nanotechnology has revolutionized the field of cancer treatment, particularly in photodynamic therapy (PDT), by enhancing the effectiveness and specificity of the treatment. More effective and selective treatment is obtained by tailoring the optical and antibacterial properties of nanostructures, leading to the use of nanotechnology in new ways in optoelectronics and medicine<sup>6-8</sup>. The application of nanotechnology in PDT offers several advantages over conventional cancer therapies. Firstly, nanoparticles can be engineered to target cancer cells specifically, minimizing damage to healthy tissues. The functionalization of nanoparticles with targeting ligands enables their selective accumulation in tumor tissues, improving treatment efficacy and reducing off-target effects<sup>9</sup>. Additionally, nanoparticles can efficiently encapsulate and deliver photosensitizing agents to the tumor site, enhancing their stability and solubility. The modification and immobilization of metal oxides serve as efficient carriers for a variety of applications due to their distinctive characteristics, such as biological activity, lack of toxicity, compatibility with living organisms, stability, and absence of carcinogenic tendencies<sup>10-12</sup>. This targeted and controlled delivery of photosensitizers improves the therapeutic outcome of PDT<sup>13</sup>. In contrast, conventional cancer therapies often lack such targeting capabilities, leading to systemic

<sup>1</sup>Faculty of Physics, Semnan University, PO Box: 35195-363, Semnan, Iran. <sup>2</sup>Department of Anatomy and Histology, College of Medicine, University of Babylon, Babylon, Iraq. <sup>3</sup>Department of Medical Biotechnology, College of Biotechnology, Al Qasim Green University, Babylon 51013, Iraq. ✉email: m\_aliannezhadi@semnan.ac.ir

toxicity and damage to healthy cells. The utilization of nanotechnology in PDT has demonstrated significant potential in advancing cancer treatment strategies<sup>14</sup>.

Titanium-based nanotubes (TNTs) have exhibited a prominent role in advanced photodynamic therapy (PDT). These nanomaterials possess unique properties, including high surface area, customizable dimensions, and excellent biocompatibility, making them well-suited for drug delivery and therapeutic applications<sup>2</sup>. In PDT, TNTs can serve as photosensitizers alone or as carriers for photosensitizing agents (nanoparticles loaded with photosensitizers). The high surface area of TNTs enables a larger loading capacity, facilitating the efficient delivery of photosensitizers to the tumor site. Furthermore, TNTs can be functionalized with targeting ligands, enhancing their selective uptake by cancer cells, thereby improving treatment specificity and minimizing damage to healthy tissues<sup>15,16</sup>.

$\text{H}_2\text{Ti}_3\text{O}_7$  nanotubes (NTs) typically have a higher surface area compared to  $\text{TiO}_2$  nanotubes, which can lead to improved catalytic activity and reactivity. Also, it leads to enhanced photocatalytic properties and superior photocatalytic properties of  $\text{H}_2\text{Ti}_3\text{O}_7$  NTs compared to  $\text{TiO}_2$  NTs, which makes them more effective in processes like cancer treatment, water purification, and pollutant degradation.  $\text{H}_2\text{Ti}_3\text{O}_7$  NTs can facilitate better charge separation and migration of photoinduced charge carriers, leading to enhanced electron-hole pair utilization in photocatalytic reactions. Also,  $\text{H}_2\text{Ti}_3\text{O}_7$  NTs offer the possibility of tuning their properties through doping, surface modifications, or varying synthesis conditions, providing flexibility for specific applications and all the mentioned advantages of  $\text{H}_2\text{Ti}_3\text{O}_7$  nanotubes over  $\text{TiO}_2$  nanotubes make them promising candidates for various applications in areas like non-invasive cancer treatment, environmental remediation, energy conversion, and sensor technology. Jiménez et al. have synthesized and engineered novel and cost-effective photo-responsive folate-conjugated titania and alumina nanotubes, showcasing responsiveness in the visible light spectrum<sup>17</sup>. Their results demonstrated that the nanocomposites exhibit photodynamic activity under visible light irradiation, whereas the folate-free nanotubes show a negligible photo-response under identical conditions. Furthermore, utilizing the same formulation, the photodynamic efficacy of folate-conjugated materials as inhibitors of cell proliferation has been demonstrated after 1 h of visible light irradiation (at 450 nm,  $100 \text{ Wm}^{-2}$ ) in 4 mg/mL solid suspensions. Zhang et al. have produced four different types of titanium oxide nanofibers (NFs) to treat HeLa cells using UV light, and the NFs especially mixed-phased NFs have shown significant lethal for killing HeLa cells and high PDT efficiencies achieved using the photosensitizers<sup>18</sup>. The enhanced photodynamic therapy (PDT) efficiency of the mixed-phase nanofibers in treating HeLa cells can be attributed to the alignment of bandgap edges and the stable interface between  $\text{TiO}_2(\text{B})$  and anatase phases within a single nanofiber. This configuration inhibits the recombination of photogenerated electrons and holes, leading to facilitating charge separation and increasing the production of reactive oxygen species (ROS). Moreover, Moosavi et al. have prepared N-doped titania nanoparticles and used them to treat Leukemia K562 cells under visible light<sup>19</sup>. They demonstrated the direct dependence of treatment efficiency on nanoparticle concentration and visible light doses. Maher et al. has reported that the interaction of laser light with  $\text{H}_2\text{Ti}_3\text{O}_7$  NTs (with a mean crystallite size of 16.0 nm) in the vicinity of lung and prostate cancer and the effects of various concentrations of bare  $\text{H}_2\text{Ti}_3\text{O}_7$  NTs at different incubation times, laser fluence, and laser wavelength to estimate the effectiveness of the photodynamic therapy by the NTs<sup>3</sup>. Treating lung and prostate cancers (A549 cells and LNCap cells) was the main goal of the paper and their results indicated that  $\text{H}_2\text{Ti}_3\text{O}_7$  NTs can be a promising candidate for treating lung and prostate cancers.

Gold nanoparticles (Au NPs) coated on metal oxide nanoparticles like titania nanotubes ( $\text{TiO}_2$  NTs) have emerged as a promising combination to obtain synergic effects of photodynamic (PDT) and photothermal (PTT) therapy in cancer treatment. The integration of Au NPs with  $\text{TiO}_2$  nanotubes offers synergistic benefits for enhanced PDT. Au NPs possess unique plasmonic properties, such as localized surface plasmon resonance (LSPR), which can enhance the generation of reactive oxygen species (ROS) during PDT<sup>20</sup>. The coating of Au NPs onto  $\text{TiO}_2$  NTs provides dual functionality,  $\text{TiO}_2$  acting as a carrier for photosensitizers and Au NPs acting as enhancers for ROS generation and light absorption leading to PTT. Additionally, the surface plasmon resonance of Au NPs enables improved light absorption and energy transfer to the surrounding photosensitizers, resulting in enhanced therapeutic effects. Au NPs can absorb incident light and turn into powerful sources of heat and ablation of tumors<sup>21,22</sup>. Therefore, adding Au NPs to  $\text{H}_2\text{Ti}_3\text{O}_7$  NTs can be an excellent choice to achieve better results in non-invasive treatments. For instance, Zhu et al. found that gold nanoparticles decorated titania nanotubes exhibit enhanced antibacterial activity and a preferable effect in stopping the growth of *Escherichia coli* and *Staphylococcus aureus* even in dark conditions which was attributed to the photocatalytic memory effect<sup>23</sup>. Yang et al. have synthesized carbon-nanodot coated on  $\text{TiO}_2$  nanotubes and used them for photodynamic therapy under a laser beam at 650 nm in vitro and in vivo assays<sup>24</sup>. They found that the nanocomposite was an excellent therapeutic agent and the reason for its success was explained by them.

According to the mentioned advantages, in the paper, a novel and facile photodynamic and photothermal agent based on gold and  $\text{H}_2\text{Ti}_3\text{O}_7$  nanotubes (Au- $\text{H}_2\text{Ti}_3\text{O}_7$  NTs) is proposed to treat prostate and lung cancers through dark and laser irradiation conditions. According to the authors' best knowledge, no reports can be found in the scientific literature on the investigation of the nanostructure in non-invasive cancer treatment until now. The results declare the success of these nanoparticles in non-invasive cancer treatment, especially prostate cancer (LNCap cells), and introduce it as a worthy candidate for the treatment.

## Material and method

### Synthesis and characterization of Au- $\text{H}_2\text{Ti}_3\text{O}_7$ NTs

In the first step,  $\text{H}_2\text{Ti}_3\text{O}_7$  NTs were synthesized using the method reported in<sup>2</sup> and then the co-precipitation method was employed to add Au nanoparticles and provide Au- $\text{H}_2\text{Ti}_3\text{O}_7$  NTs<sup>25</sup>. The characterization of Au- $\text{H}_2\text{Ti}_3\text{O}_7$  NTs was conducted through the Takram N1-541 Raman spectrometer and Shimadzu 8400 S Fourier transform infrared (FTIR) spectrometer to explore the structure and vibration modes of Au- $\text{H}_2\text{Ti}_3\text{O}_7$  NTs. The crystalline structure of Au- $\text{H}_2\text{Ti}_3\text{O}_7$  NTs was investigated by X-ray diffraction (XRD), ADVANCE-D8 model,

with Cuka radiation source ( $\lambda = 1.5406 \text{ \AA}$ ) using silicon as a standard reference material. Also, morphology and elemental compositions of the nanostructure were determined by Field emission scanning electron microscopy (FESEM), and dispersive X-ray analysis (EDX) using the TESCAN model MIRA3 microscope. Transmission electron microscopy (TEM) was done by transmission electron microscope of PHILIPS EM 208. Optical properties of Au-H<sub>2</sub>Ti<sub>3</sub>O<sub>7</sub> NTs were investigated using an ultraviolet-visible-infrared (UV-Vis-IR) spectrometer, Shimadzu UV-165 PC double-beam spectrophotometer, and diffuse reflectance spectroscopy (DRS), Avaspec-2048-TEC device. The zeta potential, hydrodynamic particle size, and suspension stability were measured using Malvern Zetasizer Nano ZS (London, UK). Differential scanning calorimetry (DSC), thermogravimetric analysis (TGA), and differential thermal analysis (DTA) were done on the Au-H<sub>2</sub>Ti<sub>3</sub>O<sub>7</sub> NTs using LINSEIS 70/2171 device to investigate the thermal stability of the sample.

### Cell culture of prostate cancer (LNCap) and lung cancer (A549)

The frozen vials contained prostate, lung, and Vero cell lines acquired from the tissue culture laboratory at the College of Medicine, University of Babylon, and the growth was maintained in a 25 ml culture flask with a complete growth medium containing 10% FBS and antibiotics, and incubated at 37 °C. Crystal violet assay as a useful method was applied to measure the cytotoxic effect of photo biomodulation using Au-H<sub>2</sub>Ti<sub>3</sub>O<sub>7</sub> NTs on different cell lines in dark conditions and under laser irradiation. The three types of cell lines including normal (Vero) cells, lung (A549), and prostate (LNCap) cancer cells were seeded in 96-well plates with  $5 \times 10^5$  cells/well of density and incubated at 37 °C for 24 h. Then, cells including normal and cancer cells (lung and prostate cells) were treated with different concentrations of Au-H<sub>2</sub>Ti<sub>3</sub>O<sub>7</sub> NTs (15.6–500 µg/ml). After each experiment, the medium was discarded and the cells were washed with 100 µL of cold PBS, then 100 µL of 0.5% crystal violet staining solution was added to each well. After an incubation time of 20 min at room temperature, the plate was washed three times with tap water. Afterward, the cytotoxicity was measured according to reference<sup>2,26,27</sup> for each well with a microtiter plate reader at the optical wavelength of 570 nm.

### Laser irradiation of cells incubated with Au-H<sub>2</sub>Ti<sub>3</sub>O<sub>7</sub> NTs

Laser irradiation was applied to incubated Au-H<sub>2</sub>Ti<sub>3</sub>O<sub>7</sub> NTs to investigate the cytotoxic effect of photo-biomodulation on different cells. The three types of cell lines including normal (Vero) cells, lung (A549), and prostate (LNCap) cancer cells were seeded in 96-well plates with  $5 \times 10^5$  cells/well of density and incubated at 37 °C for 24 h. Cells were treated with different concentrations of Au-H<sub>2</sub>Ti<sub>3</sub>O<sub>7</sub> NTs (15.6–500 µg/ml) on normal and cancer cells (lung and prostate cells) under laser irradiations at different fluence and wavelengths (near IR at  $\lambda = 808 \text{ nm}$ , red laser at  $\lambda = 635 \text{ nm}$ , and green laser at  $\lambda = 532 \text{ nm}$ ). The laser was positioned vertically above each well at a distance of 10 cm from the bottom of the plate<sup>28</sup>. The energy density (fluence) (J/cm<sup>2</sup>) was calculated by multiplying the exposure time (s) by the laser power density W/cm<sup>2</sup>. After each experiment, the medium was discarded and cells were washed with 100 µL of cold PBS and then 100 µL of 0.5% crystal violet staining solution was added to each well. After an incubation time of 20 min at room temperature, the plate was washed three times with tap water. Afterward, the cytotoxicity was measured according to reference<sup>26,27</sup> for each well with a microtiter plate reader at the optical wavelength of 570 nm.

## Results and discussion

### Chemical structure and vibration modes

To inform about the chemical structure and vibration modes of the nanostructures, Fourier-transform infrared (FTIR) spectroscopy was carried out and the spectrum of the sample is displayed in Fig. 1a in the range of 400–4000 cm<sup>-1</sup>. Five absorption peaks located at wavenumbers 445, 690, 912, 1637, and 3454 cm<sup>-1</sup> can be seen in the spectrum. The absorption peak centered at 445 and 690 cm<sup>-1</sup> are attributed to the stretching vibrations of Ti–O–Ti bonds<sup>29</sup> and the peak at 960 cm<sup>-1</sup> is due to the presence of Ti–O bond in the sample<sup>30</sup> which demonstrates the formation of titanium oxide molecules in the sample. The sharp and intense peak at 1636 cm<sup>-1</sup> and broad absorption peak in the range of 2900–3700 cm<sup>-1</sup> are related to the molecular water bending mode of water Ti–OH and stretching vibration of –OH from absorbed water, respectively<sup>31,32</sup>. This FTIR absorption peak related to Ti–OH vibration declares the formation of hydrated titanium oxides in the sample.

To find more information about the bonds created in the hydrated titanium oxide sample and confirm the FTIR results, Raman spectroscopy was applied to the sample, and the Raman spectrum is shown in Fig. 1b. Several peaks can be observed in the Raman spectrum of the sample. To obtain precise information about the chemical bonds of the sample, the Raman spectrum can be deconvoluted into individual Gaussian peaks using Origin software and fitting multi-Gaussian functions to the Raman spectrum. The constitutive Gaussian functions (green solid lines) are also plotted in Fig. 1b, and the center of each Gaussian peak is mentioned at the top of the peak. The Raman spectrum of the sample has several major (175.6, 442.8, and 733.0 cm<sup>-1</sup>) and minor (109.4, 513.7, 559.0, 827.8, and 827.8 cm<sup>-1</sup>) peaks related to 2E<sub>g</sub> (276), E<sub>g</sub> (443 cm<sup>-1</sup>), A<sub>1g</sub> (559), 2B<sub>1g</sub>(733 cm<sup>-1</sup>), and 2B<sub>1g</sub> + E<sub>g</sub> (912 cm<sup>-1</sup>) of site symmetries of the Ti and O which interpreted by using the group theory<sup>33,34</sup>.

The conjugating gold to H<sub>2</sub>Ti<sub>3</sub>O<sub>7</sub> NTs changes the bond energy, leading to a difference in the Raman shift of the peaks in Fig. 1b compared to H<sub>2</sub>Ti<sub>3</sub>O<sub>7</sub> NTs in reference<sup>2</sup>. However, there is no evidence of gold in the FTIR or Raman spectra which is due to no molecular bond related to gold atoms. So, FTIR and Raman spectroscopies cannot confirm the existence of gold in the samples and other analyses should prove it. In addition, the intensity and full width at half maximum (FWHM) of the constituent Gaussian components are a measure of the crystalline properties, and higher crystallinity causes higher intensity and lower FWHM of the peaks. Therefore, a comparison of the Raman spectra of the samples with the H<sub>2</sub>Ti<sub>3</sub>O<sub>7</sub> NTs in reference<sup>2</sup> reveals the formation of partly the same structure. Furthermore, the obtained intensity of the Raman peaks for the current sample is lower than the structure in<sup>2</sup> due to the existence of gold atoms in the structure, and less crystalline order of hydrated titanium oxides in the current structure. In addition, the partly small difference between the Raman

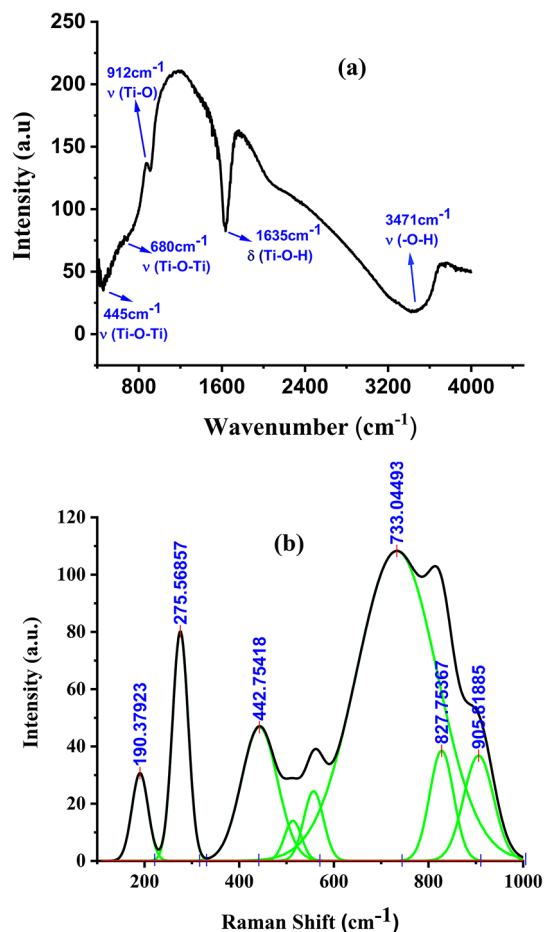


**Fig. 1.** (a) Fourier-transform infrared (FTIR) and (b) Raman spectra of the Au-hydrated titanium oxides.

peak shift of the constituent components obtained for the current sample compared to the  $\text{H}_2\text{Ti}_3\text{O}_7$  NTs occurs due to the different chemical bond lengths of these two types of molecules which can happen due to various reasons such as the existence of gold molecules in the structures, different nanoparticle size, crystalline phase and size of the nanoparticles.

### Crystallinity

The XRD pattern of the sample is depicted in Fig. 2. The pattern was analyzed by X'Pert High Score Plus software and it was compatible with the standard card 00-041-0192. It is demonstrated that the diffraction peaks labeled by stars, \*, are associated with monoclinic hydrogen titanium oxide,  $\text{H}_2\text{Ti}_3\text{O}_7$ , with the lattice parameters of  $a = 15.990 \text{ \AA}$ ,  $b = 3.738 \text{ \AA}$ ,  $c = 9.172 \text{ \AA}$  which is consistent with the results of previous analysis (chemical structure and vibration modes studies). Also, according to the standard card 96-901-1613, a sharp peak labeled by diamond at  $2\theta = 38.27^\circ$  is related to the cubic phase of Au with the lattice parameters of  $a = b = c = 4.0650 \text{ \AA}$  and space group of  $Fm\bar{3}m$  which verify the existence of Au and its crystalline nature in the sample.

Furthermore, to estimate the mean crystallite size of the sample, the XRD pattern of the Au- $\text{H}_2\text{Ti}_3\text{O}_7$  sample is considered using the Scherrer equation ( $d_{sh} = k\lambda/(\beta \cos \theta)$ ), where,  $K$  and  $\lambda$  are shape factor and X-ray radiation's wavelength ( $1.5418 \text{ \AA}$ ); and  $d$ ,  $\theta$ , and  $\beta$  are the mean crystallite size, the Bragg angle, and the FWHM (full width at half maximum) of the main diffraction peak, respectively<sup>35,36</sup>. The mean crystallite size of hydrogen titanium oxide ((310) plane) and Au ((111) plane) are  $44.2 \text{ \AA}$  and  $329.4 \text{ \AA}$ , respectively.

Also, the specific surface area (SSA) of the Au- $\text{H}_2\text{Ti}_3\text{O}_7$  sample can be calculated in dense and monodispersed nanoparticles approximation by  $SSA = 6/(\rho \times d)$ , where  $\rho$  is the particle density of hydrogen titanium oxide and Au which are  $3.19$  and  $19.97 \text{ gr/cm}^3$  according to standard card 00-041-0192 and 96-901-1613 of X'Pert high score software. The calculated SSA values of hydrogen titanium oxide and Au are  $42.5 \text{ m}^2/\text{g}$  and  $0.92 \text{ m}^2/\text{g}$ , respectively.

### Morphology

Field emission scanning electron microscopy (FESEM) images of Au- $\text{H}_2\text{Ti}_3\text{O}_7$  sample with two different magnifications are shown in Fig. 3a to study the morphology of the nanostructure. The results confirm the growth of rod-like or maybe nanotube nanostructures. Furthermore, the low magnification FESEM image of the sample in the inset of Fig. 3a indicates the uniformity of the formed nanostructure. Furthermore, the average

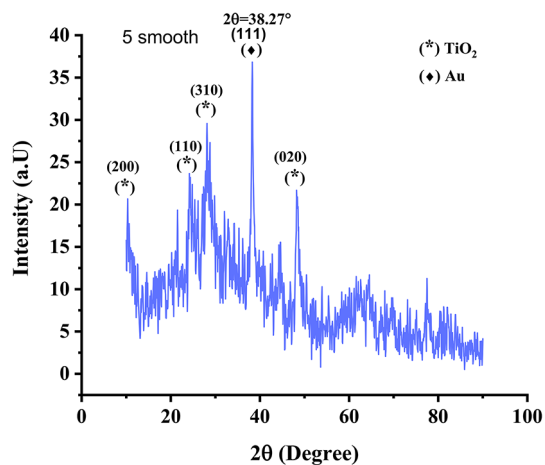


Fig. 2. X-ray diffraction pattern of Au-H<sub>2</sub>Ti<sub>3</sub>O<sub>7</sub>.

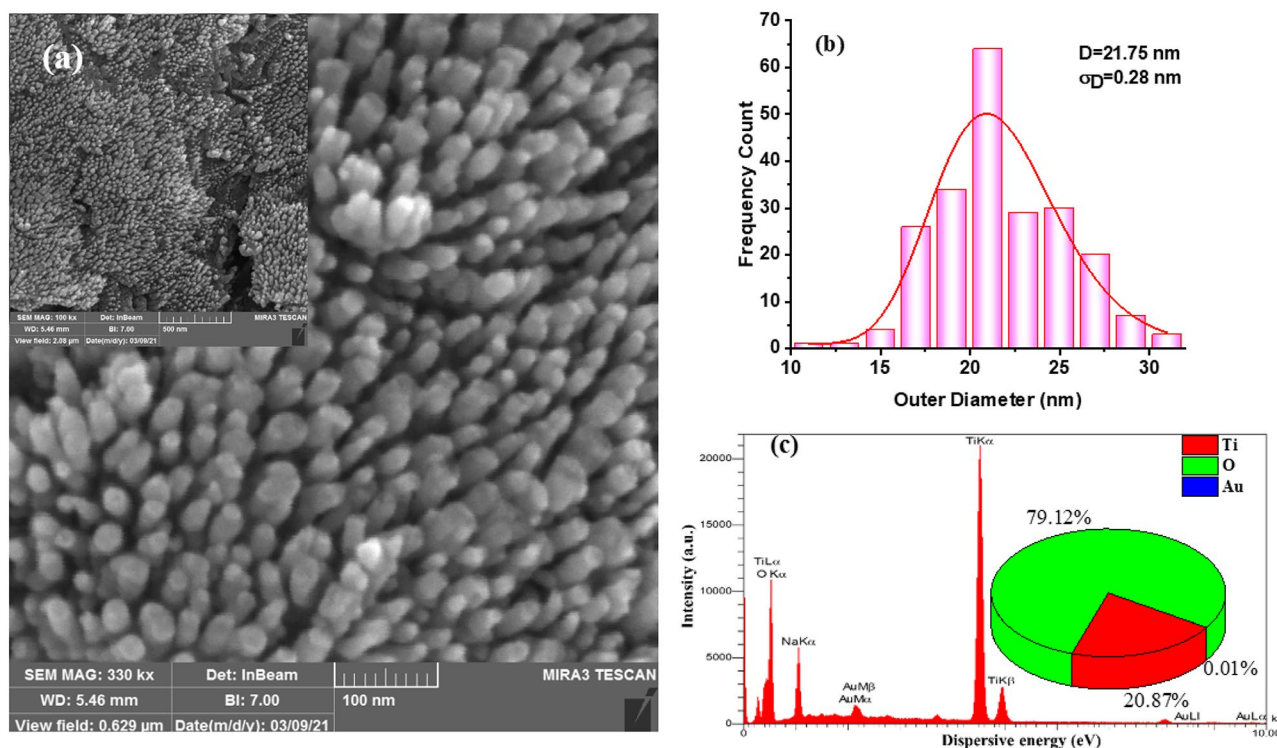


Fig. 3. (a) Field emission scanning electron microscopy (FESEM) images with two different magnifications, (b) The distribution histogram of nanorods diameters, and (c) energy dispersive X-ray plot (EDX) including the atomic percentages of the elements detected in the Au-H<sub>2</sub>Ti<sub>3</sub>O<sub>7</sub> nanostructure. The fitting log-normal function to the distribution histogram of nanostructure diameters is shown with a solid red line in the histogram plot.

diameter of the Au-H<sub>2</sub>Ti<sub>3</sub>O<sub>7</sub> sample,  $\langle d \rangle$ , and data dispersion,  $\sigma_D$ , may be calculated using Digimizer software by fitting the following log-normal function in Origin software<sup>37–39</sup>:

$$y(x) = y_0 + \frac{A}{\sqrt{2\pi wx}} \exp\left(\frac{\ln\left(\frac{x}{x_0}\right)^2}{2w^2}\right) \quad (1)$$

$$\langle d \rangle = x_0 \exp\left(\frac{w^2}{2}\right) \quad (2)$$

$$\sigma_D = \langle d \rangle (\exp w^2 - 1)^{\frac{1}{2}} \quad (3)$$

where  $x$  denotes the diameter or other dimensional quantities of nanostructure that are desirable to measure.  $y$  is the frequency count of every size, and  $x_0$ ,  $y_0$ , and  $w$  are also fitting parameters obtained by fitting the log-normal function to the distribution histogram of the desirable dimension of the nanostructures as mentioned in Fig. 3b. The average diameter of nanorods is  $21.75 \pm 0.28$  nm, which indicates the uniformity of Au-H<sub>2</sub>Ti<sub>3</sub>O<sub>7</sub> nanostructure.

For further investigation, transmission electron microscopy (TEM) analysis was done on the sample, and high and low magnifications TEM images are shown in Fig. 4a,b. The results declare that Au-H<sub>2</sub>Ti<sub>3</sub>O<sub>7</sub> NTs were grown. The distribution histogram of shell thickness and the outer diameter of the Au-H<sub>2</sub>Ti<sub>3</sub>O<sub>7</sub>NTs and log-normal functions fitted to data are presented in Fig. 4c,d. The calculated average shell thickness and the outer diameter of the nanotubes are equal to  $2.24 \pm 0.03$  nm and  $7.10 \pm 0.12$  nm, respectively. Furthermore, data dispersion percentages of nanotube shell thickness and the outer diameter are 1.25% and 1.72%, respectively, which confirm the good quality of the nanostructure used in the research. As you can observe, the estimated average of outer diameters obtained using FESEM and TEM images are different, which is due to the lower accuracy of FESEM analysis compared to TEM analysis and the inability of FESEM in identifying and distinguishing the Au-H<sub>2</sub>Ti<sub>3</sub>O<sub>7</sub> nanotubes.

EDX analysis was done on Au-H<sub>2</sub>Ti<sub>3</sub>O<sub>7</sub> nanotubes to investigate its chemical elements and the result is shown in Fig. 3c. The result confirms the existence of Ti, O, and Au in the sample with atomic percentages of 20.87%, 79.12%, and 0.01%, respectively, with no undesirable elements in the sample meaning the purity of the Au-H<sub>2</sub>Ti<sub>3</sub>O<sub>7</sub> nanotubes.

### Optical properties

The absorption and reflection spectra of Au-H<sub>2</sub>Ti<sub>3</sub>O<sub>7</sub> nanotubes are the most important optical quantities, especially in phenomena related to the interactions of light with nanostructure, such as cancer treatment with photothermal and/or photodynamic therapies or even wastewater treatment by photodegradation of dyes or else<sup>40</sup>. Diffuse reflectance spectroscopy (DRS) and UV-Vis-NIR spectroscopy are also two common methods for studying the optical properties of nanostructures that were carried out to investigate the optical properties of Au-H<sub>2</sub>Ti<sub>3</sub>O<sub>7</sub> NTs and the results are depicted in Fig. 5a,b, respectively. According to Fig. 5a, the absorption of Au-H<sub>2</sub>Ti<sub>3</sub>O<sub>7</sub> NTs contains two peaks centered at 249 and 435 nm, and the first one is more intense. The first absorption peak is related to the absorption of H<sub>2</sub>Ti<sub>3</sub>O<sub>7</sub> nanotubes and the second is due to the LSPR phenomenon occurring in gold nanoparticles. The lower absorption peak at 435 nm compared to 249 nm can be understood by the lower value of gold in the Au-H<sub>2</sub>Ti<sub>3</sub>O<sub>7</sub> NTs compared to H<sub>2</sub>Ti<sub>3</sub>O<sub>7</sub>, which was demonstrated by the EDX analysis results (0.01% of Au and 79.12% of Ti in the sample).

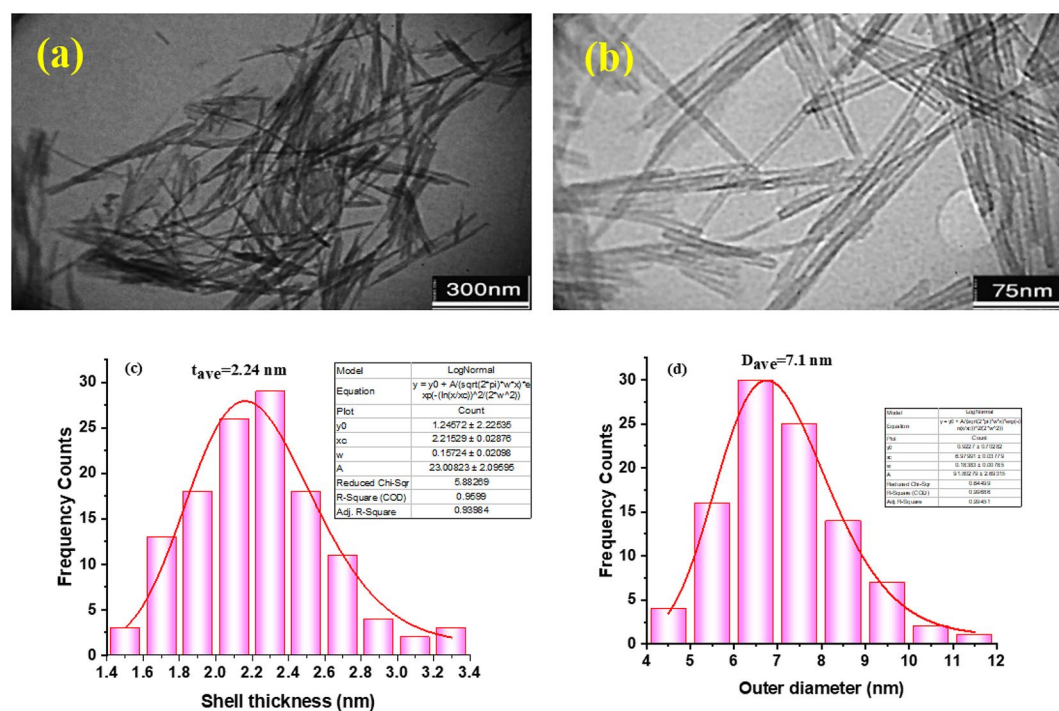


**Fig. 4.** (a and b) Transmission electron microscopy (TEM) plots of Au- H<sub>2</sub>Ti<sub>3</sub>O<sub>7</sub> nanotubes in two different magnifications, the distribution histogram of (c) shell thickness and (d) outer diameter of Au- H<sub>2</sub>Ti<sub>3</sub>O<sub>7</sub> nanotubes with fitted log-normal functions.

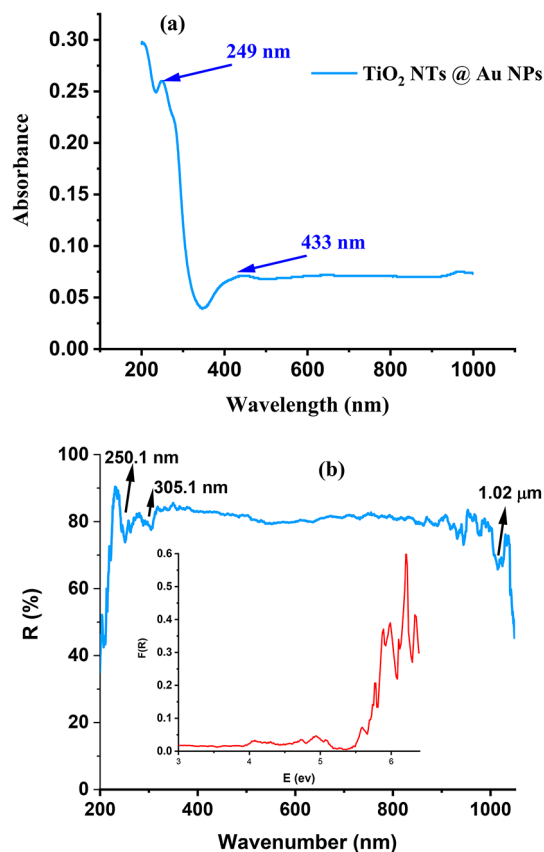


**Fig. 5.** (a) Absorption and (b) reflection spectra of the Au-H<sub>2</sub>Ti<sub>3</sub>O<sub>7</sub> NTs using UV-Vis-NIR and DRS spectroscopy data, respectively. The Kubelka-Munk function versus photon energy is plotted in the inset of (b) with a solid red line.

Also, the sample reflectance in Fig. 5b shows that the reflectance of the Au-H<sub>2</sub>Ti<sub>3</sub>O<sub>7</sub> NTs in the visible region is about 80%. In addition, significant low reflections are observed around the wavelengths of 200 nm ( $R \sim 40\%$ ) and 1.02 microns ( $R \sim 65\%$ ) which are mentioned in the inset of Fig. 5b. The Kubelka-Munk function,  $F(R)$ , is proportional to the absorption coefficient,  $\alpha$ , and the function can be calculated using equation  $F(R) = (1 - R^2)/(2R)$ <sup>41,42</sup>, where  $R$  is the reflection coefficient of the Au-H<sub>2</sub>Ti<sub>3</sub>O<sub>7</sub> NTs. The Kubelka-Munk function versus photon energy is plotted in the inset of Fig. 5b and it reveals that most absorptions occur at high energies and in the ultraviolet region.

Also, the Tauc method using the equation  $(\alpha E)^m = B(E - E_g)$  is usually used to calculate the bandgap energy<sup>35,43</sup> of the nanopowders and it can be applied to DRS or UV-Vis-NIR spectroscopy data to obtain the direct and indirect energy gap of the Au-H<sub>2</sub>Ti<sub>3</sub>O<sub>7</sub> NTs. Here,  $E$  and  $E_g$  are photon energy and bandgap energy of the Au-H<sub>2</sub>Ti<sub>3</sub>O<sub>7</sub> NTs, respectively,  $B$  is a constant,  $m$  is 2 and  $\frac{1}{2}$  for calculating the direct and indirect energy bandgaps, respectively, and  $\alpha$  is the absorption of the Au-H<sub>2</sub>Ti<sub>3</sub>O<sub>7</sub> NTs. Also, the calculated Kubelka-Munk function using DRS data can be used instead of absorption in the mentioned equation. The  $(\alpha h\nu)^2$  and  $(\alpha h\nu)^{1/2}$  versus photon energy are plotted in Fig. 6a,b using UV-Vis-NIR and DRS data and then the straight lines are fitted to each Tauc plot to determine the direct and indirect bandgap energies of Au-H<sub>2</sub>Ti<sub>3</sub>O<sub>7</sub> NTs. According to the obtained results from both methods, the Au-H<sub>2</sub>Ti<sub>3</sub>O<sub>7</sub> NTs is an indirect semiconductor with a bandgap energy in the range of 3.37 eV (Fig. 6a) to 3.75 eV (Fig. 6b). The calculated direct and indirect energy gaps using these two spectroscopies' data are slightly different due to different measurement methods, and also experimental and computational errors.

### Stability of nanoparticles in suspension

Zeta potential analysis, which investigates electrokinetic potential in colloidal systems or colloid-electrolyte interactions, is a significant characterization technique used to estimate the surface charge of nanoparticles. It can provide some vital information about the physical stability of nanosuspensions. Zeta potential values are typically in the range of  $-100$  mV to  $+100$  mV<sup>44</sup> and a large positive (more than  $+30$  mV) or negative (less than  $-30$  mV) value of nanoparticles zeta potential meaning good physical stability of nanosuspensions due to sufficient electrostatic repulsion of individual particles<sup>45</sup>. Furthermore, particle aggregation, flocculation, and physical colloidal instability can occur due to insufficient repulsive electrokinetic force (in the range of  $-30$  mV to  $30$  mV) to overcome Van der Waals as an attractive force at zeta potentials. It should be noted that the potential zeta interval  $-30$  to  $+30$  is not a definite interval for the instability of nanoparticles and in many

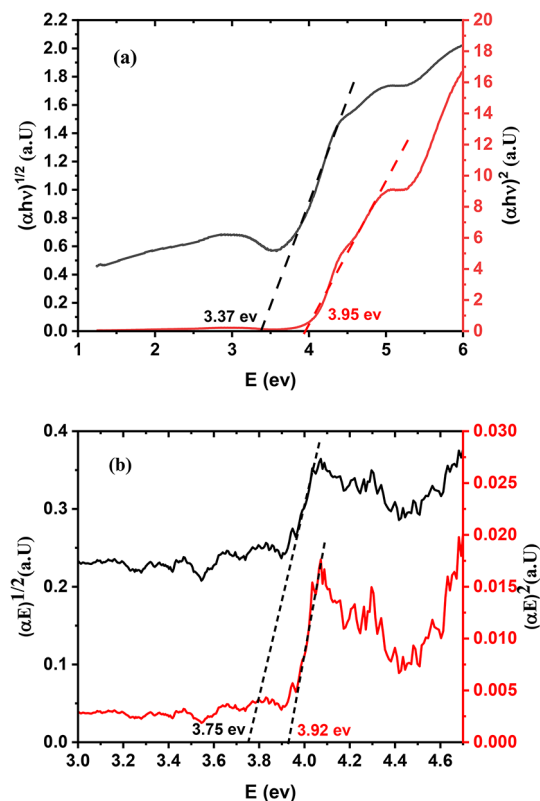


**Fig. 6.** Tauc plot of Au-H<sub>2</sub>Ti<sub>3</sub>O<sub>7</sub> NTs by using (a) UV-Vis NIR transmittance spectroscopy data and (b) diffuse reflectance spectroscopy (DRS) data to calculate direct and indirect energy gaps. The linear solid lines are fitted to the linear parts of the Tauc plots.

scientific literatures the potential zeta less than  $-25$  mV or more than  $+25$  mV was declared as a high degree of stability<sup>44,46</sup>.

Zeta potential analysis was done on the Au-H<sub>2</sub>Ti<sub>3</sub>O<sub>7</sub> NTs, and the result is presented in Fig. 7a. As you can observe, the zeta potential of the Au-H<sub>2</sub>Ti<sub>3</sub>O<sub>7</sub> NTs is in the range of  $-64$  mV to  $-22$  mV with a maximum total count at  $-41.4$  mV. To further investigate, the full width at half maximum (FWHM) of the zeta potential diagram obtained for the NTs is plotted in Fig. 7a and the result declares that most nanoparticles have a zeta potential in the range of  $-49$  mV to  $-32$  mV. Therefore, such high values of zeta potential guarantee high colloidal stability of nanoparticle suspension and strong electrostatic repulsive forces between Au-H<sub>2</sub>Ti<sub>3</sub>O<sub>7</sub> NTs.

Dynamic light scattering (DLS) is a commonly used method to determine the particle size of dispersed nanoparticles in liquid that has some advantages over other methods like microscopy including the possibility of in situ size determination of secondary nanoparticles in the suspension<sup>47</sup>. So, the DLS method was used to investigate the size of dispersed Au-H<sub>2</sub>Ti<sub>3</sub>O<sub>7</sub> NTs in deionized water at room temperature, and the result is presented in Fig. 7b. The size distribution diagram of Au-H<sub>2</sub>Ti<sub>3</sub>O<sub>7</sub> NTs has two peaks located at size values of 91.28 nm and 459.0 nm related to the passage of light in a direction close to the diameter and height of Au-H<sub>2</sub>Ti<sub>3</sub>O<sub>7</sub> NTs, respectively.

The differences between the average sizes of nanostructures obtained using SEM and the DLS analyses are attributed to their related concepts, principles, and inherent limitations and characteristics. DLS measures the hydrodynamic diameters of nanoparticles in solution which undergo random Brownian motion, and measures the fluctuations in scattered light due to this motion to determine the size distribution. Also, it measures the size of nanoparticles along with the thickness of the solvent or hydration layer around the nanoparticles which causes increasing the measured size compared to the SEM size of the nanoparticles. Furthermore, aggregation of nanoparticles can affect the DLS size leading to larger apparent sizes compared to SEM size of nanoparticles. On the other hand, SEM analysis provides high-resolution imaging of nanoparticles on a solid substrate, meaning measures a direct visualization of the physical size and morphology of individual nanoparticles and provides the physical dimensions of the nanoparticles on the substrate, without considering any solvent or hydration layer around the particles or aggregation. Therefore, the hydrodynamic size of nanoparticles measured by DLS is usually different from SEM sizes of nanoparticles, and it is related to the stability of nanoparticles in liquid, providing valuable information for the nanostructure applications in liquid. Therefore, the mentioned hydrodynamic size of nanoparticles is important for cancer treatment and drug delivery.

The results of zeta potential and DLS analyses suggest that Au-H<sub>2</sub>Ti<sub>3</sub>O<sub>7</sub> NTs can be a suitable candidate for further investigation in cancer treatment. However, the thermal stability of these nanoparticles should also be investigated, which will be discussed in the next subsection.



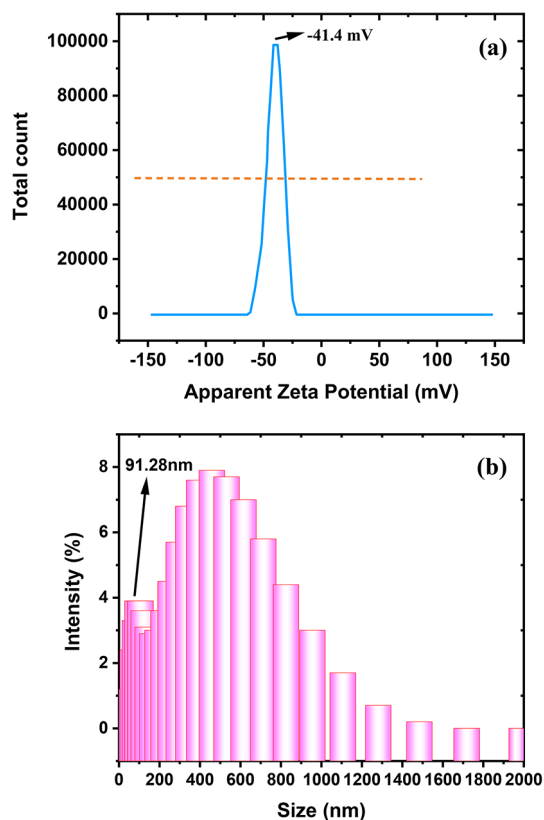


**Fig. 7.** (a) Zeta potential and (b) the size distribution diagram of Au-H<sub>2</sub>Ti<sub>3</sub>O<sub>7</sub> NTs dispersed in deionized water and measured by dynamic light scattering (DLS).

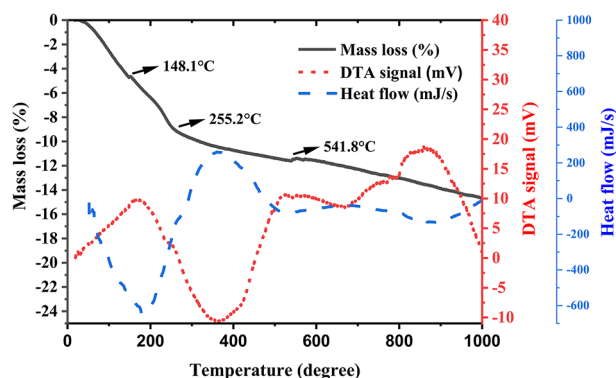


**Fig. 8.** Thermogravimetric analysis (black solid line), differential thermal analysis (red short dash line), and differential scanning calorimetry (blue dash line) of Au-H<sub>2</sub>Ti<sub>3</sub>O<sub>7</sub> NTs in an air atmosphere with a heating rate of 10.4 °C / min.

### Thermal stability

Thermogravimetric analysis (TGA) is a less expensive, fast, and easy analysis to investigate the change in the physical and chemical properties of the nanostructures or to determine the thermal stability. So, the analysis was performed on Au-H<sub>2</sub>Ti<sub>3</sub>O<sub>7</sub> NTs in an air atmosphere with a heating rate of 10.4 °C/min, and the results are presented in Fig. 8 with a black solid line. Also, differential thermal analysis (DTA) and differential scanning calorimetry (DSC) are two partly similar thermoanalytical techniques that measure the difference between sample and reference temperatures and record them to achieve some information about either exothermic or endothermic processes such as glass transitions, crystallization, melting and sublimation in the nanomaterial. Therefore, DTA and DSC analyses were performed on Au-H<sub>2</sub>Ti<sub>3</sub>O<sub>7</sub> NTs and the results are shown in Fig. 8 with a red short dash line and a blue dash line, respectively. These three curves can be used together to obtain comprehensive information about the thermal behavior of Au-H<sub>2</sub>Ti<sub>3</sub>O<sub>7</sub> NTs.

Typically, a reduction in mass is discernible across all segments of the thermogravimetric analysis (TGA) plot but the slope of the curve varies in different parts. Initially, an endothermic reaction occurs with increasing the temperature that involves the liberation of unbound water into the pores or surface of the Au-H<sub>2</sub>Ti<sub>3</sub>O<sub>7</sub> NTs. The mass loss percentage during this process (up to 148.1 °C) reaches -4.7%. After that, some reactions occur and the water inside the bond is removed. This result is consistent with FTIR spectroscopy, which demonstrates the presence of free water and hydrated structure. The crystallization processes of the structure occur at temperatures of 283.1, 364.5, 541.8, 664, 768, 796, and 851 °C as exothermic processes. The exothermic peaks around 283.1, 364.5, and 541.8 °C are probably related to phase changes and the formation of anatase phases of titanium oxide nanostructures<sup>48–51</sup>. Furthermore, a distinct exothermic peak at 664 °C is attributed to the phase transition of titanium oxide nanostructures from anatase to rutile phases<sup>52</sup>. Finally, the total mass loss present of Au-H<sub>2</sub>Ti<sub>3</sub>O<sub>7</sub> NTs is about 14.6%, which declares that the sample has good thermal stability. Also, the thermal analysis diagram of these nanotubes is different from the H<sub>2</sub>Ti<sub>3</sub>O<sub>7</sub> nanotubes<sup>2</sup> and some fluctuations can be observed in the DTA signal and heat flux curves, which can be attributed to the presence of a small amount of gold in the recent Au-H<sub>2</sub>Ti<sub>3</sub>O<sub>7</sub> NTs.

### Cell viability

In this section, different concentrations of Au-H<sub>2</sub>Ti<sub>3</sub>O<sub>7</sub> NTs are applied on different normal and cancer cells to investigate their side effect on normal cells and their treatment effects on lung and prostate cancer cells. Studies are divided into two main parts: the first explores the impact of Au-H<sub>2</sub>Ti<sub>3</sub>O<sub>7</sub> nanotubes independently under dark conditions, and the second explores the combined effect of the nanotubes and the interaction of laser radiation with the nanotubes, focusing on photodynamic and photothermal therapies. Tests are also performed on Vero, A549, and LNCap upon different incubation times (24 and 48 h) at 37 °C with different lasers including NIR (808 nm), red (635 nm), and green (532 nm) lasers and the results are presented in this section.

#### *The effect of Au-H<sub>2</sub>Ti<sub>3</sub>O<sub>7</sub> NTs on the normal cells, lung, and prostate cancer cells (dark conditions)*

The cultured Vero cells were incubated with different concentrations of Au-H<sub>2</sub>Ti<sub>3</sub>O<sub>7</sub> NTs at 37 °C for 24 h and then the cell viability% and cytotoxicity%, which are just labeled with viability% and cytotoxicity% for simplicity, were estimated using crystal violet as follows<sup>27</sup> and the results are presented in Fig. 9a:

$$Viability\% = \frac{OD\ of\ test}{OD\ of\ control} \times 100 \quad (6)$$

$$Cytotoxicity\% = 100\% - Viability\% \quad (7)$$

where *OD of test* and *OD of control* are the optical densities of the test (or treated cells) and control (untreated cells) samples, respectively.

According to the results of Fig. 9a, incubation of normal (Vero) cells with Au-H<sub>2</sub>Ti<sub>3</sub>O<sub>7</sub> NTs has no significant effect on viability%, and viability% is about 100% even up to high concentrations of these nanotubes meaning that the threshold limit or the border concentration of NTs for significant cell death and side effects on normal cells is more than 400 µg/mL.

The same tests were done on A549, and LNCap cells using different concentrations of the Au-H<sub>2</sub>Ti<sub>3</sub>O<sub>7</sub> NTs upon different incubation times of 24 (for A549 and LNCap cells) and 48 (for LNCap cells) hours and the results are depicted in Fig. 9b, c, respectively. Results of Fig. 9b demonstrate that low concentrations of Au-H<sub>2</sub>Ti<sub>3</sub>O<sub>7</sub> NTs (15.6 and 32.25 µg/mL) exhibit negligible impacts on the viability of A549 cells. However, higher concentrations lead to a reduction in viability percentage, with levels reaching approximately 80% and 70% for incubations with 62.5 and 500 µg/mL of the proposed Au-H<sub>2</sub>Ti<sub>3</sub>O<sub>7</sub> NTs at a temperature of 37 °C for 24 h. Also, results of Fig. 9c indicate that Au-H<sub>2</sub>Ti<sub>3</sub>O<sub>7</sub> NTs have more effect on LNCap cells in dark conditions compared to A549 cells, and viability% decrease significantly even with the lowest NTs concentration (15.6 µg/mL) and incubation time of 24 h and it reaches ~80% which previously obtained with the higher concentration of NTs (4 times larger) in the A549 cells. Also, the viability% of LNCap cells with the highest concentration of Au-H<sub>2</sub>Ti<sub>3</sub>O<sub>7</sub> NTs (500 µg/mL) and incubation time of 24 h is 59.1%. It means that almost half of the prostate cancer cells died with the Au-H<sub>2</sub>Ti<sub>3</sub>O<sub>7</sub> NTs without any external sources like LED light or laser light during a short incubation time (24 h). Moreover, increasing the incubation time to 48 h leads to a severe drop in viability% at all concentrations, so the viability% of the cells using the lowest and higher concentrations of NTs are 42% and less than 22%, respectively, meaning the NTs presented an IC<sub>50</sub> value of less than 15.6 µg/mL in LNCap cells for this treatment conditions.

value of about 500 µg/mL. The viability % of LNCap cells reaches 16% for the highest concentration of NTs (500 µg/mL), which means the death of almost all prostate cancer cells in dark conditions using Au-H<sub>2</sub>Ti<sub>3</sub>O<sub>7</sub> NTs and incubation time of 48 h. These interesting results were not obtained with the previously proposed NTs (bare H<sub>2</sub>Ti<sub>3</sub>O<sub>7</sub> NTs) on these two cancer cells<sup>2</sup>.

The reasons for these phenomena can be described as follows: tumor blood vessels in cancer cells often have a defective cellular lining composed of disorganized, loosely connected, branched, overlapping, or sprouting endothelial cells which makes tumor endothelium very leaky. In addition, tumors with poorly developed lymphatic drainage allow accumulation of nano-sized materials in cancer cells compared to normal cells such as accumulation of nanomaterials with long time called enhanced permeability and retention effect (EPR), and photosensitizers can also be covalently bonded to several biomolecules including antibodies, proteins, carbohydrates, and others, that the biomolecules have an affinity to tumors. Antitumor effects of NTs affected by NPs size, aggregation tendency, and accumulation, which are key factors that determine cell viability and genetic alteration in tumor cells<sup>53</sup>, and even the type of disease may substantially change the biological identity of NPs and their biological fates, including their cellular uptake and toxicity<sup>54</sup>.

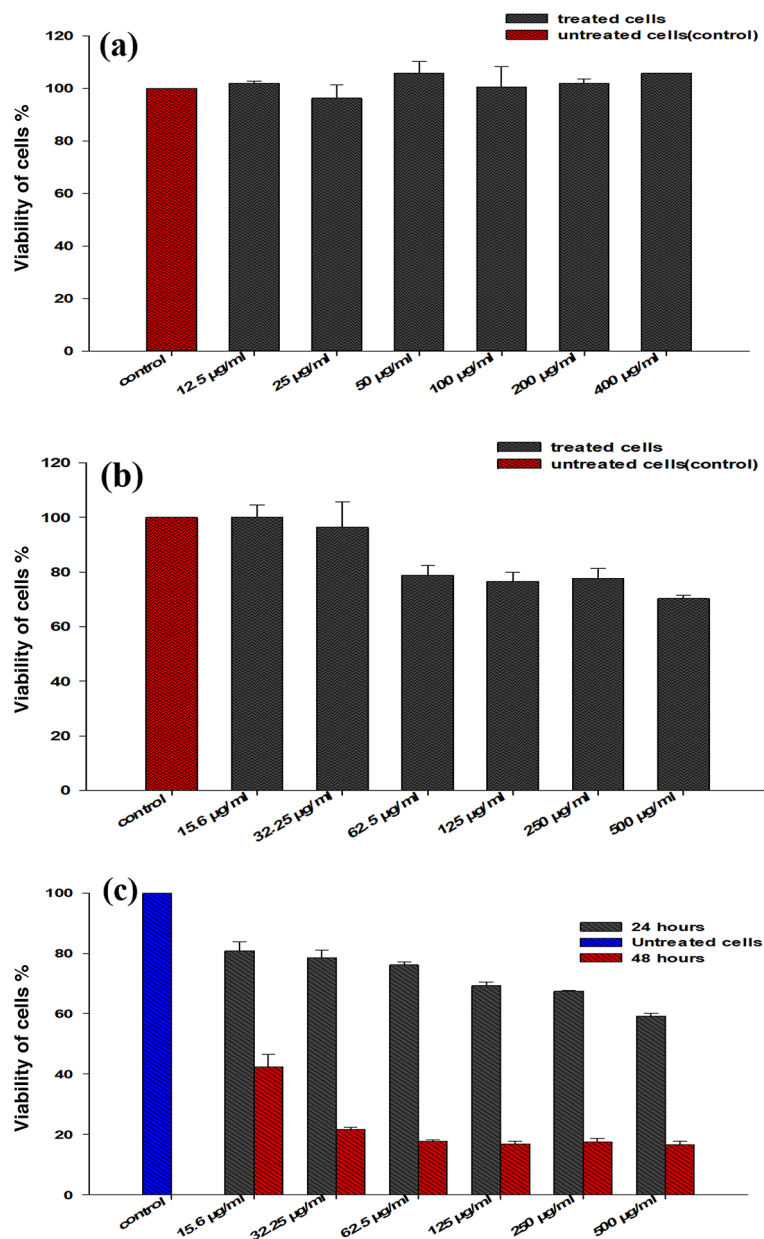


**Fig. 9.** Effect of Au-H<sub>2</sub>Ti<sub>3</sub>O<sub>7</sub> NTs on (a) normal cells (Vero cells) with incubation time of 24 h, (b) lung cancer cells (A549 cells) with incubation time of 24 h, and (c) prostate cancer cells (LNCap cells) upon incubation with different times of 24 and 48 h at 37 °C (dark condition).

Hence, the findings are particularly encouraging as the Au-H<sub>2</sub>Ti<sub>3</sub>O<sub>7</sub> nanotubes demonstrate no impact on healthy cells, yet exhibit a substantial effect on cancer cells. In other words, these nanoparticles have a selective effect on cancer cells and greatly reduce the viability % during incubation times 24 and 48 h and it can be an excellent candidate for more research on non-invasive lung and prostate cancer treatments through the interaction of laser beams with the Au-H<sub>2</sub>Ti<sub>3</sub>O<sub>7</sub> NTs in the vicinity of cancer cells to use the synergistic enhancement of the phototherapeutic efficiency.

#### *The effect of laser beam on Au-H<sub>2</sub>Ti<sub>3</sub>O<sub>7</sub> NTs in vicinity of cancer cells*

In this section, the effects of different laser irradiations including NIR (808 nm), green (532 nm), and red (635 nm) lasers on Au-H<sub>2</sub>Ti<sub>3</sub>O<sub>7</sub> NTs embedded in the lung (A549 cells) and prostate cancer cells (LNCap cells) are investigated to study the abilities of using the interactions of laser beams with Au-H<sub>2</sub>Ti<sub>3</sub>O<sub>7</sub> NTs for cancer treatment.

**Lung cancer (A549 cells)** First, the synergistic photodynamic and photothermal effects of irradiated Au-H<sub>2</sub>Ti<sub>3</sub>O<sub>7</sub> NTs (with a red diode laser at 635 nm) on lung cancer cells are investigated and optical inverted microscope images of lung cancer (A549 cells) embedded with the different concentrations of NTs (62.5 and 500 µg/

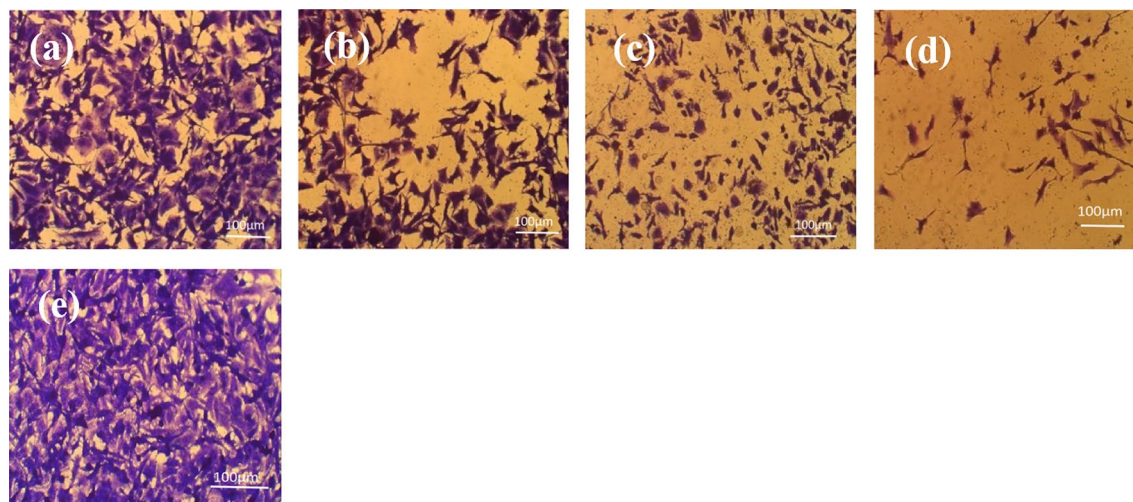


**Fig. 10.** Optical inverted microscope images of lung cancer (A549 cells) embedded with Au-H<sub>2</sub>Ti<sub>3</sub>O<sub>7</sub> NTs with concentrations of (a and c) 62.5 µg/ml, and (b and d) 500 µg/ml irradiated by a diode laser at a wavelength of 635 nm and fluence of (a and b) 72.5 J/cm<sup>2</sup> and (c and d) 365 J/cm<sup>2</sup> and incubated at 37 °C for 24 h. For comparison, an optical inverted microscope image of the control group cells is also plotted in (e).

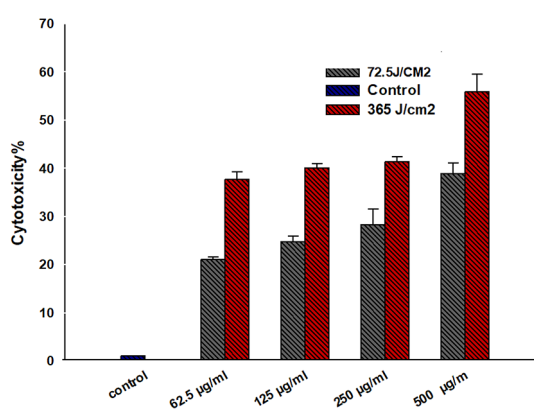


**Fig. 11.** Dependence of Au-H<sub>2</sub>Ti<sub>3</sub>O<sub>7</sub> NTs cytotoxicity% on the concentration of NTs and laser fluence provided by a red diode laser at 635 nm during the treatment of A549 cells.

ml) and irradiated with different red laser fluence (72.5 J/cm<sup>2</sup> and 365 J/cm<sup>2</sup>) are presented in Fig. 10 at the incubation time of 24 h. For comparison, an optical inverted microscope image of the control group cells is also presented in Fig. 10e. The results of Fig. 10 declare that increasing the concentration of Au-H<sub>2</sub>Ti<sub>3</sub>O<sub>7</sub> NTs and laser fluence has reduced the cell viability, significantly. The cell viability% of A549 cells after treatment with irradiated 500 µg/ml of Au-H<sub>2</sub>Ti<sub>3</sub>O<sub>7</sub> NTs with a red laser beam with a fluence of 365 J/cm<sup>2</sup> (Fig. 10d) is very small compared to the control group (Fig. 10e). Therefore, this treatment can be effective on lung cancer cells.

Furthermore, for quantitative analysis, cytotoxicity histograms of A549 cells treated with different concentrations of irradiated Au-H<sub>2</sub>Ti<sub>3</sub>O<sub>7</sub> NTs by a diode laser at 635 nm with different laser fluence (72.5 and 365 J/cm<sup>2</sup>) are presented in Fig. 11. For the study, crystal violet assay was performed on A549 cells just 24 h after laser irradiation, and the cytotoxicity% was calculated according to Eq. 7. The results reveal that increasing the concentration of Au-H<sub>2</sub>Ti<sub>3</sub>O<sub>7</sub> NTs in both laser fluences does not have a notable impact on the cytotoxicity of A549 cells and increasing the concentration of NTs from 62.5 to 250 µg/ml in laser fluence 72.72 J/cm<sup>2</sup> and 365 J/cm<sup>2</sup> resulted in a change in cytotoxicity% from 21.1 to 28.3% and 37.6 to 41.3%, respectively.

In the studied concentrations range, the highest cytotoxicity% is related to using 500 mg/ml of Au-H<sub>2</sub>Ti<sub>3</sub>O<sub>7</sub> NTs that are equal to 39.0% and 55.9% for laser fluence of 72.72 J/cm<sup>2</sup> and 365 J/cm<sup>2</sup>, respectively. In addition, increasing the laser fluence causes an increase in cytotoxicity of the Au-H<sub>2</sub>Ti<sub>3</sub>O<sub>7</sub> NTs, and the NTs presented an IC<sub>50</sub> value of 375 mg/ml in A549 cells using a laser fluence of 365 J/cm<sup>2</sup>.

**3.7.2.2 Prostate cancer (LNCap cells)** In this section, the effects of different lasers including NIR (808 nm) and green (532 nm) lasers are investigated on embedded Au-H<sub>2</sub>Ti<sub>3</sub>O<sub>7</sub> NTs in prostate cancer cells (LNCap cells), and the efficiencies of the proposed prostate cancer treatment are studied.

**NIR laser** NIR laser at a wavelength of 808 nm, power of 2 W, and fluence of 214.2 J/cm<sup>2</sup> was applied on Au-H<sub>2</sub>Ti<sub>3</sub>O<sub>7</sub> NTs -embedded LNCap cells, and the cells incubated at 37 °C for 24 h. Then, the cell viability assay using crystal violet was recorded, and the results are shown in Fig. 12a. Initial observations suggest that exposing a high-power NIR laser on Au-H<sub>2</sub>Ti<sub>3</sub>O<sub>7</sub> NTs surrounded by LNCap cells has no significant effects on the cancer cells, as evidenced by the nearly unchanged cell viability percentages. This phenomenon can be explained by the high diffuse reflection (80.9%) and low light absorbance (0.07) of the NTs at 808 nm. However, taking a closer look and comparing the results with Fig. 9b reveals that the cell viability% of LNCap cells by irradiated Au-H<sub>2</sub>Ti<sub>3</sub>O<sub>7</sub> NTs-embedded LNCap cells (95.8%, 93.1%, 89.4%, and 74.9% for NTs concentration of 62.5, 125, 250, and 500 µg/mL) is even higher than the viability% of Au-H<sub>2</sub>Ti<sub>3</sub>O<sub>7</sub> NTs-embedded LNCap cells in the dark condition (76.1%, 69.3%, 67.5%, and 59.2% for NTs concentration of 62.5, 125, 250, and 500 µg/mL), where cancer cells are just incubated with Au-H<sub>2</sub>Ti<sub>3</sub>O<sub>7</sub> NTs without applying any light. Therefore, in this process, two competing phenomena emerge, one leading to a decline in the viability of LNCap cells while the other contributes to its enhancement.

For a better and more comprehensive understanding of the phenomena, a parallel experiment was conducted using the H<sub>2</sub>Ti<sub>3</sub>O<sub>7</sub> nanotubes previously introduced in reference<sup>2</sup>, and the results are depicted in Fig. 12a. Cell viability% of LNCap cells in the vicinity of irradiated Au-H<sub>2</sub>Ti<sub>3</sub>O<sub>7</sub> NTs-embedded (85.2%, 86.0%, 86.8%, and 82.9% for H<sub>2</sub>Ti<sub>3</sub>O<sub>7</sub> NTs concentration of 62.5, 125, 250, and 500 µg/mL) is higher than its viability% in the vicinity H<sub>2</sub>Ti<sub>3</sub>O<sub>7</sub> NTs in dark condition in reference<sup>2</sup>, too. Therefore, for more clarity, the quantity  $V_r = V_{NIR\ Laser} - V_{dark}$  is defined, where  $V_{NIR\ Laser}$  and  $V_{dark}$  are viability% of LNCap cells in the vicinity of irradiated and dark NTs-embedded, respectively.  $V_r$  of LNCap cells versus NTs concentration and well-fitted parabola functions is depicted in Fig. 12b. It can be observed that  $V_r$  is positive for the treatment of prostate cancers with two studied NTs and all NTs concentrations, which means that the viability% of LNCap cells treated by irradiated NTs is usually more than the viability% of LNCap cells embedded by both H<sub>2</sub>Ti<sub>3</sub>O<sub>7</sub> NTs and Au-H<sub>2</sub>Ti<sub>3</sub>O<sub>7</sub> NTs in dark conditions. This may be due to the reason that the NIR laser radiation makes LNCap cells more aggressive and it means the NIR irradiation may be an unsuitable candidate for LNCap cell treatment which should be more investigated.

**Green laser** The optical penetration depth of NIR laser beams is more than visible laser beams. However, the results indicate that exposing the NIR laser beam to H<sub>2</sub>Ti<sub>3</sub>O<sub>7</sub> NTs and Au-H<sub>2</sub>Ti<sub>3</sub>O<sub>7</sub> NTs-embedded LNCap cells does not cause successful treatment, and even dark conditions cause better results compared to NIR irradiation

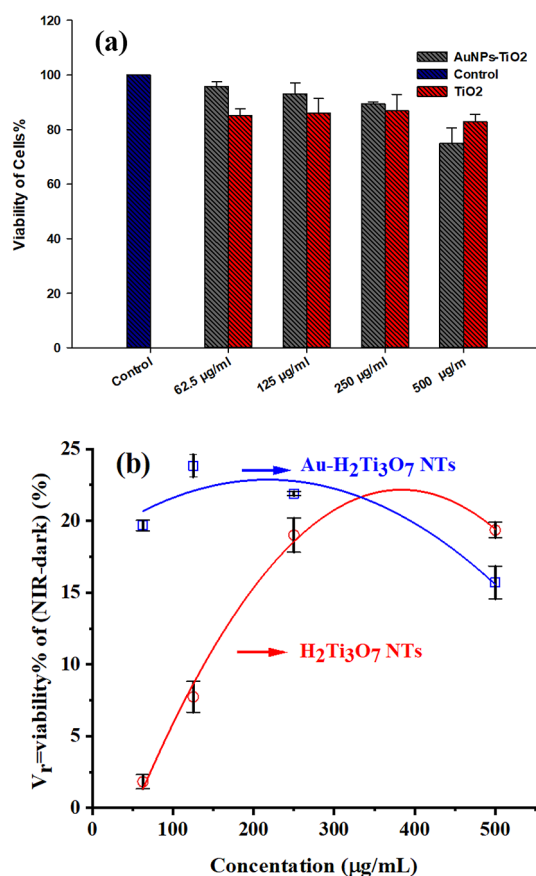


**Fig. 12.** (a) Dependence of prostate LNCap cells viability% to irradiated H<sub>2</sub>Ti<sub>3</sub>O<sub>7</sub> NTs and Au-H<sub>2</sub>Ti<sub>3</sub>O<sub>7</sub> NTs concentrations by a NIR laser at a wavelength of 808 nm, laser power of 2 W, and laser fluence of 214.2 J/cm<sup>2</sup> and (b) Vr of LNCap cells versus NTs concentrations.

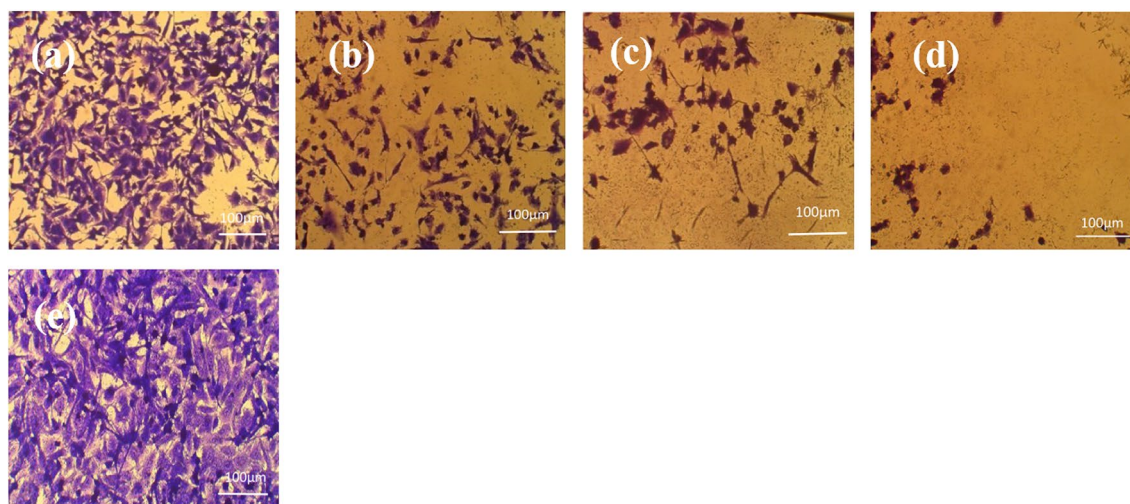


**Fig. 13.** Optical inverted microscope images of cancer prostate (LNCap cells) embedded by Au-H<sub>2</sub>Ti<sub>3</sub>O<sub>7</sub> NTs with concentrations of (a and c) 62.5 µg/ml, and (b and d) 500 µg/ml irradiated by a laser at a wavelength of 532 nm and fluence of 450 J/cm<sup>2</sup>. The LNCap cells were incubated for (a and b) 24 h and (c and d) 48 h at 37 °C. For comparison, optical inverted microscope images of the control group cells are also plotted in Fig. 10e.

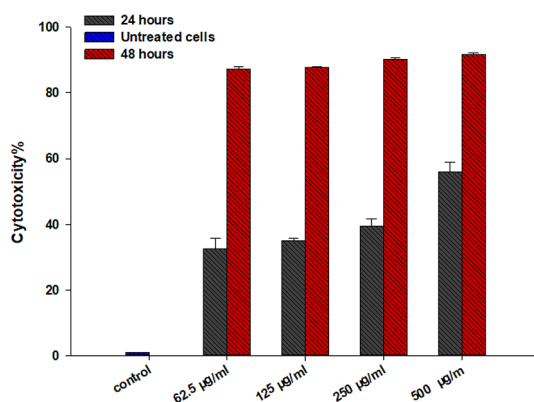


**Fig. 14.** Dependence of irradiated Au-H<sub>2</sub>Ti<sub>3</sub>O<sub>7</sub> NTs cytotoxicity in prostate LNCap on the concentrations of NTs irradiated by a green laser at a wavelength of 532 nm and fluence of 450 J/cm<sup>2</sup>. The cells were incubated at 37 °C at two incubation times of 24 and 48 h.

conditions. Therefore, in the next step, the effects of Nd: YAG laser irradiation at 532 nm with a fluence of 450 J/cm<sup>2</sup> are investigated in vitro on Au-H<sub>2</sub>Ti<sub>3</sub>O<sub>7</sub> NTs-embedded LNCap cells to achieve better treatment conditions for prostate cancer cells. The research was based on varying concentrations of Au-H<sub>2</sub>Ti<sub>3</sub>O<sub>7</sub> nanotubes integrated into LNCap cells and exposure to green laser beams in 24- and 48-hour incubation at 37 °C. The treatment results were recorded with two different concentrations of NTs (62.5 µg/ml and 500 µg/ml) and two different incubation times (24 and 48 h) and optical inverted microscope images of prostate cancer (LNCap cells) including irradiated Au-H<sub>2</sub>Ti<sub>3</sub>O<sub>7</sub> NTs by green laser are shown in Fig. 13. Also, an optical inverted microscope image of the control group cells is presented in Fig. 13e to compare. The results demonstrate that prostate cancer (LNCap cells) treatments by exposing a laser beam at 532 nm to Au-H<sub>2</sub>Ti<sub>3</sub>O<sub>7</sub> NTs are significantly successful and can meaningfully reduce the viability% of prostate cancer cells so that the treatment with this laser and the NTs concentration of 500 µg/mL almost results in complete cell death (Fig. 13d). Also, a comparison of the results in Fig. 13a with b and 13c with d shows that increasing the concentration of Au-H<sub>2</sub>Ti<sub>3</sub>O<sub>7</sub> NTs from 62.5 g/mL to 500 g/mL leads to a significant decrease in cell viability of LNCap cells. Furthermore, the comparison of the results of 13a with c and also 13b with d shows that increasing the incubation time has a great effect on reducing the cell viability.

For a more qualitative and detailed investigation, cytotoxicity% of prostate cancer (LNCap cells) cells under treatment by the interaction of a green laser beam with a fluence of 450 J/cm<sup>2</sup> with different concentrations of Au-H<sub>2</sub>Ti<sub>3</sub>O<sub>7</sub> NTs were obtained and the results are depicted in Fig. 14. The results declare that cell viabilities% of (67.0%, 64.7%, 60.3%, and 43.8) and (12.5%, 12.1%, 9.4%, and 8.1%) are provided in the case of the treatment of

prostate cancer cells by exposing the green laser irradiating to Au-H<sub>2</sub>Ti<sub>3</sub>O<sub>7</sub> NTs with the concentration of (62.5, 125, 250, and 500 µg/mL) at incubation times of 24 and 48 h, respectively. Therefore, increasing the concentrations of the proposed NTs and incubation times improves the outcome of the prostate cancer treatment. However, the effect of increasing the incubation time on the treatment is much greater, so that increasing the incubation time from 24 to 48 h (two times) at lower concentrations even causes an increase in cytotoxicity% up to three times and it increases up to two times at highest concentrations of 500 µg/m. Also, the NTs presented IC50 values of 375 µg/mL and much smaller than 62.5 µg/mL in LNCap cells for the laser fluence of 450 J/cm<sup>2</sup> at 24 and 48 h incubation times, respectively.

Finally, the results confirm that near-complete destruction of prostate cancer cells is provided by exposing a green laser light with a fluence of 450 J/cm<sup>2</sup> to 500 µg/mL Au-H<sub>2</sub>Ti<sub>3</sub>O<sub>7</sub> NTs embedded in LNCap cells and an incubation time of 48 h. Therefore, Au-H<sub>2</sub>Ti<sub>3</sub>O<sub>7</sub> NTs and these treatment conditions can be applied in non-invasive prostate cancer treatment.

## Conclusion

Cancer treatment and water treatment are two important global challenges that can be addressed through the interaction of light with nanoparticles including metal oxide nanoparticles, plasmonic nanoparticles, or both. Significant efficiencies of bare H<sub>2</sub>Ti<sub>3</sub>O<sub>7</sub> NTs in the treatment of prostate and lung cancers were previously reported by exposing the red and green laser beams<sup>2</sup>. In the paper, Au-H<sub>2</sub>Ti<sub>3</sub>O<sub>7</sub> NTs were proposed to treat prostate and lung cancers in dark and irradiated conditions. The reasons behind selecting the nanoparticles and studying the interaction of lasers with the NTs embedded in the special cancer cells are to use the synergic effects of H<sub>2</sub>Ti<sub>3</sub>O<sub>7</sub> NTs and Au. Au NPs and H<sub>2</sub>Ti<sub>3</sub>O<sub>7</sub> NTs as powerful plasmonic nanoparticles and metal oxide can provide the PTT and PDT, respectively. It can be observed that the interaction of laser light wavelength with cancer cells and also inorganic Au-H<sub>2</sub>Ti<sub>3</sub>O<sub>7</sub> NTs can affect the treatment efficiency, and choosing the laser wavelength is very important in the success of prostate cancer treatment. conventional laser therapy using a NIR laser at 808 nm led to cancer cell invasion and the failure of prostate cancer treatment while using the 532 nm laser produced astonishing treatment results. A comparison of the current treatment results with H<sub>2</sub>Ti<sub>3</sub>O<sub>7</sub> NTs in reference<sup>2</sup> for prostate cancer (LNCap cells) in the same condition declares that increasing gold to H<sub>2</sub>Ti<sub>3</sub>O<sub>7</sub> NTs improves the efficiency of prostate cancer treatment significantly, while exposing a red laser beam to H<sub>2</sub>Ti<sub>3</sub>O<sub>7</sub> NTs-embedded lung cancer leads a more efficient cancer treatment compare to treatment using Au-H<sub>2</sub>Ti<sub>3</sub>O<sub>7</sub> NTs.

Furthermore, it was found that a laser wavelength of 532 nm is close to the LSPR wavelength of gold nanoparticles in Au-H<sub>2</sub>Ti<sub>3</sub>O<sub>7</sub> NTs. Therefore, green light-induced ROS production of the Au-H<sub>2</sub>Ti<sub>3</sub>O<sub>7</sub> NTs increases due to LSPR-induced hot electrons and heat generation. The combination of PDT and PTT treatments with Au-H<sub>2</sub>Ti<sub>3</sub>O<sub>7</sub> NTs has great potential to be applied to cancer treatment and to improve the treatment efficiency, especially for LNCap prostate cells. The results are motivating because Au-H<sub>2</sub>Ti<sub>3</sub>O<sub>7</sub> does not impact healthy cells, while significantly influencing cancer cells. In other words, these nanoparticles have a selective effect on cancer cells and greatly reduce the viability % during incubation times 24 and 48 h and it can be an excellent candidate for non-invasive lung and prostate cancer treatments.

## Data availability

All data included in this paper are available upon request by contact with the contact corresponding author.

Received: 24 March 2024; Accepted: 8 October 2024

Published online: 29 October 2024

## References

- Dolmans, D. E., Fukumura, D. & Jain, R. K. Photodynamic therapy for cancer. *Nat. Rev. Cancer.* **3**(5), 380–387. <https://doi.org/10.1038/nrc1071> (2003).
- Al-Shemri, M. I., Aliannezhadi, M., Al-Awady, M. J. & Ghaleb, R. A. Interaction of different lasers beams with synthesized H<sub>2</sub>Ti<sub>3</sub>O<sub>7</sub> nanotubes: toward photodynamic therapy. *Opt. Quant. Electron.* **55**, 671. <https://doi.org/10.1007/s11082-023-04977-5> (2023).
- Guo, Q. et al. Current treatments for non-small cell lung cancer. *Front. Oncol.* **12**, 945102. <https://doi.org/10.3389/fonc.2022.945102> (2022).
- Alvarez, N. & Sevilla, A. Current advances in photodynamic therapy (PDT) and the future potential of PDT-Combinatorial Cancer therapies. *Int. J. Mol. Sci.* **25**(2), 1023. <https://doi.org/10.3390/ijms25021023> (2024).
- Singh, N., Gupta, R. S. & Bose, S. A comprehensive review on singlet oxygen generation in nanomaterials and conjugated polymers for photodynamic therapy in the treatment of cancer. *Nanoscale.* <https://doi.org/10.1039/D3NR05801H> (2024).
- Azadmehr, S., Fadavieslam, M. R., Tafreshi, M. J. & Alamdari, S. Substrate and cu concentration-dependent physical properties of spray-deposited Cu<sub>2</sub>ZnSnS<sub>4</sub> thin films: a comparative study. *J. Mater. Sci.: Mater. Electron.* **35**(12), 855. <https://doi.org/10.1007/s10854-024-12499-3> (2024).
- Alamdari, S., Mansourian, M. & Ghamsari, M. S. Thin Ga-doped ZnO Film with enhanced dual visible lines Emission. *Curr. Nanomater.* **9**(3), 279–285. <https://doi.org/10.2174/2405461508666230829102228> (2024).
- Saadabadi, R. H., Tehrani, F. S., Darroudi, M. & Sabouri, Z. Plant-based synthesis of ZnO–CeO<sub>2</sub>–MgO nanocomposite using *Ocimum Basilicum* L seed extract: Biological effects and photocatalytic activity. *Mater. Chem. Phys.* **314**, 128919. <https://doi.org/10.1016/j.matchemphys.2024.128919> (2024).
- Peer, D. et al. Nanocarriers as an emerging platform for cancer therapy. *Nano-enabled Med. Appl.* 61–91, (2020).
- Valinezhad, N., Talebi, A. F. & Alamdari, S. Biosynthesize, physicochemical characterization and biological investigations of chitosan-Ferula gummosa essential oil (CS-FEO) nanocomposite. *Int. J. Biol. Macromol.* **241**, 124503. <https://doi.org/10.1016/j.jbiomac.2023.124503> (2023).
- Alamdari, S., Mirzaee, O., Tafreshi, M. & Riedel, R. Immobilization of ZnO: Ga nanocrystals in a polystyrene/cellulose matrix: a novel hybrid nanocomposite photocatalyst for future photo energy application. *Compos. Part. B: Eng.* **265**, 110934. <https://doi.org/10.1016/j.compositesb.2023.110934> (2023).

12. Alamdari, S. et al. Green synthesis of multifunctional ZnO/chitosan nanocomposite film using wild *Mentha pulegium* extract for packaging applications. *Surf. Interfaces*. **34**, 102349. <https://doi.org/10.1016/j.surfin.2022.102349> (2022).
13. Altery, S. S., Mostafa, G. A., El-Tohamy, M. F. & AlRabia, H. New Enhancement Spectrofluorimetric Determination of Anti-Breast Cancer Drugs Palbociclib by Biogenic-Synthesized Alumina/NiO Nanocomposite, *ChemistrySelect*, **9**(10), e202304586, <https://doi.org/10.1002/slct.202304586> (2024).
14. Lucky, S. S., Soo, K. C. & Zhang, Y. Nanoparticles in photodynamic therapy, *Chem. Rev.* **115**(4), 1990–2042, <https://doi.org/10.1021/cr5004198> (2015).
15. Wang, X., Zhong, X. & Cheng, L. Titanium-based nanomaterials for cancer theranostics. *Coord. Chem. Rev.* **430**, 213662. <https://doi.org/10.1016/j.ccr.2020.213662> (2021).
16. Shang, L., Zhou, X., Zhang, J., Shi, Y. & Zhong, L. Metal nanoparticles for photodynamic therapy: A potential treatment for breast cancer, *Molecules* **26**(21), 6532, <https://doi.org/10.3390/molecules26216532> (2021).
17. Jiménez, V. A. et al. Visible-light-responsive folate-conjugated titania and alumina nanotubes for photodynamic therapy applications. *J. Mater. Sci.* **55**(16), 6976–6991. <https://doi.org/10.1007/s10853-020-04483-z> (2020).
18. Zhang, S. et al. Enhanced photodynamic therapy of mixed phase TiO<sub>2</sub>(B)/anatase nanofibers for killing of HeLa cells. *Nano Res.*, **7**(11), 1659–1669, <https://doi.org/10.1007/s12274-014-0526-8> (2014).
19. Moosavi, M. A. et al. Photodynamic N-TiO<sub>2</sub> nanoparticle treatment induces controlled ROS-mediated autophagy and terminal differentiation of leukemia cells, *Sci. Rep.* **6**(1), 34413, <https://doi.org/10.1038/srep34413> (2016).
20. Saha, K., Agasti, S. S., Kim, C., Li, X. & Rotello, V. M. Gold nanoparticles in chemical and biological sensing. *Chem. Rev.* **112**(5), 2739–2779. <https://doi.org/10.1021/cr2001178> (2012).
21. Hainfeld, J. F. et al. Infrared-transparent gold nanoparticles converted by tumors to infrared absorbers cure tumors in mice by photothermal therapy. *PLoS One*. **9**(2), e88414. <https://doi.org/10.1371/journal.pone.0088414> (2014).
22. Khan, S., Alam, F., Azam, A. & Khan, A. U. Gold nanoparticles enhance methylene blue-induced photodynamic therapy: a novel therapeutic approach to inhibit *Candida albicans* biofilm. *Int. J. Nanomed.* 3245–3257. <https://doi.org/10.2147/IJN.S31219> (2012).
23. Zhu, H. et al. Gold nanoparticles decorated titanium oxide nanotubes with enhanced antibacterial activity driven by photocatalytic memory effect, *Coatings* **12**(9), 1351, <https://doi.org/10.3390/coatings12091351> (2022).
24. Yang, D. et al. Carbon-dot-decorated TiO<sub>2</sub> nanotubes toward photodynamic therapy based on water-splitting mechanism. *Adv. Healthc. Mater.* **7**(10), 1800042. <https://doi.org/10.1002/adhm.201800042> (2018).
25. Salimi, Z., Ehsani, M., Dezfuli, A. S. & Alamzadeh, Z. Evaluation of Iron and Au-Fe 3 O 4 Ferrite Nanoparticles for Biomedical Application. *J. Supercond. Novel Magn.* 1–8. <https://doi.org/10.1007/s10948-021-06012-8> (2022).
26. Al-Shreefy, H. H., Al-Wasiti, E. & Al-Awady, M. Investigation of encapsulated selenium nanoparticles with PLGA polymers against MCF-7 and HBL cell lines. *Nano Biomed. Eng.* **15**(2), 105–117. <https://doi.org/10.26599/NBE.2023.9290013> (2023).
27. Feoktistova, M., Geserick, P. & Leverkus, M. Crystal violet assay for determining viability of cultured cells, *Cold Spring Harbor Protocols*, (4), pdb.prot087379, <https://doi.org/10.1101/pdb.prot087379>(2016).
28. Ghaleb, R., Naciri, M., Al-Majmaie, R., Maki, A. & Al-Rubeai, M. Enhancement of monoclonal antibody production in CHO cells by exposure to He-Ne laser radiation. *Cytotechnology* **66**, 761–767. <https://doi.org/10.1007/s10616-013-9625-8> (2014).
29. Mahalingam, T., Selvakumar, C., Kumar, E. R. & Venkatachalam, T. Structural, optical, morphological and thermal properties of TiO<sub>2</sub>-Al and TiO<sub>2</sub>-Al<sub>2</sub>O<sub>3</sub> composite powders by ball milling. *Phys. Lett. A*. **381**, 1815–1819. <https://doi.org/10.1016/j.physleta.2017.02.053> (2017).
30. Vasconcelos, D. C. L. et al. Infrared spectroscopy of titania sol-gel coatings on 316L stainless steel, <https://doi.org/10.4236/msa.2011.210186> (2011)
31. Maira, A. et al. Fourier transform infrared study of the performance of nanostructured TiO<sub>2</sub> particles for the photocatalytic oxidation of gaseous toluene. *J. Catal.* **202**(2), 413–420. <https://doi.org/10.1006/jcat.2001.3301> (2001).
32. León, A. et al. FTIR and Raman characterization of TiO<sub>2</sub> nanoparticles coated with polyethylene glycol as carrier for 2-methoxyestradiol. *Appl. Sci.* **7**(1), 49. <https://doi.org/10.3390/app7010049> (2017).
33. Yajun, J. Growth mechanism and photocatalytic performance of double-walled and bamboo-type TiO<sub>2</sub> nanotube arrays. *RSC Adv.* **4**(76), 40474–40481. <https://doi.org/10.1039/C4RA03630A> (2014).
34. Hardcastle, F. Raman spectroscopy of titania (TiO<sub>2</sub>) nanotubular water-splitting catalysts. *J. Ark. Acad. Sci.* **65**(1), 43–48. <https://doi.org/10.54119/jaas.2011.6504> (2011).
35. Gholizadeh, Z., Aliannezhadi, M., Ghominejad, M. & Shariatmadar Tehrani, F. Optical and structural properties of spherical-shaped boehmite and  $\gamma$ -alumina nanoparticles by ultrasonic-assisted hydrothermal method: the effects of synthesis route, calcination, and precursor concentration. *Opt. Quant. Electron.* **55**(10), 880. <https://doi.org/10.1007/s11082-023-05157-1> (2023).
36. Aliannezhadi, M., Doostmohamadi, F., Jamali, M. & Tehrani, F. S. The interaction of light with oxygen-vacancy-rich W18O<sub>49</sub> nanoparticles synthesized using different acid molarities for acidic and neutral water treatments. *Opt. Mater.* 115909. <https://doi.org/10.1016/j.optmat.2024.115909> (2024).
37. Aliannezhadi, M., Mirsanai, S. Z., Jamali, M. & Tehrani, F. S. Optical and structural properties of bare MoO<sub>3</sub> nanobelt, ZnO nanoflakes, and MoO<sub>3</sub>/ZnO nanocomposites: the effect of hydrothermal reaction times and molar ratios. *Opt. Mater.* **147**, 114619. <https://doi.org/10.1016/j.optmat.2023.114619> (2024).
38. Naranji, E., Aliannezhadi, M. & Panahibakhsh, S. Surface structured silver-copper bimetallic nanoparticles by irradiation of excimer laser pulses to bilayer thin films. *Phys. Scr.* **98**(10), 105529. <https://doi.org/10.1088/1402-4896/acfa38> (2023).
39. Vatani, P., Aliannezhadi, M. & Shariatmadar Tehrani, F. Improvement of optical and structural properties of ZIF-8 by producing multifunctional Zn/Co bimetallic ZIFs for wastewater treatment from copper ions and dye. *Sci. Rep.* **14**(1), 15434. <https://doi.org/10.1038/s41598-024-66276-7> (2024).
40. Aliannezhadi, M., Mirsanaee, S. Z., Jamali, M. & Shariatmadar Tehrani, F. The physical properties and photocatalytic activities of green synthesized ZnO nanostructures using different ginger extract concentrations, *Sci. Rep.* **14**(1), 2035. <https://doi.org/10.1038/s41598-024-52455-z> (2034).
41. Gholizadeh, Z., Aliannezhadi, M., Ghominejad, M. & Tehrani, F. S. High specific surface area  $\gamma$ -Al<sub>2</sub>O<sub>3</sub> nanoparticles synthesized by facile and low-cost co-precipitation method. *Sci. Rep.* **13**(1), 6131. <https://doi.org/10.1038/s41598-023-33266-0> (2023).
42. Gholizadeh, Z., Aliannezhadi, M., Ghominejad, M. & Tehrani, F. S. Novel boehmite and  $\eta$ -alumina nanostructures synthesized using a green ultrasonic-assisted hydrothermal method by clove extract for water treatment. *J. Water Process. Eng.* **65**, 105786. <https://doi.org/10.1016/j.jwpe.2024.105786> (2024).
43. Khanahmadzadeh, S., Enhessari, M., Solati, Z., Mohebalizadeh, A. & Alipouramjad, A. Synthesis, characterization and optical band gap of the Co<sub>2</sub>TiO<sub>4</sub> nanoparticles. *Mater. Sci. Semiconduct. Process.* **31**, 599–603. <https://doi.org/10.1016/j.mssp.2014.12.043> (2015).
44. Shnoudeh, A. J. et al. Synthesis, characterization, and applications of metal nanoparticles, in *Biomaterials and Bionanotechnology: Elsevier*, 527–612. (2019).
45. Joseph, E. & Singhvi, G. Multifunctional nanocrystals for cancer therapy: a potential nanocarrier, *Nanomaterials for drug delivery and therapy*, 91–116. <https://doi.org/10.1016/B978-0-12-816505-8.00007-2> (2019).
46. Sheikhi, S., Aliannezhadi, M. & Tehrani, F. S. Effect of precursor material, pH, and aging on ZnO nanoparticles synthesized by one-step sol-gel method for photodynamic and photocatalytic applications. *Eur. Phys. J. Plus.* **137**(1), 60. <https://doi.org/10.1140/epjp/s13360-021-02252-8> (2022).
47. Kato, H. Size determination of nanoparticles by dynamic light scattering. *Nanomaterials: Process. Charact. Lasers.* 535–554. <https://doi.org/10.1002/9783527646821> (2012).



48. Nithiyantham, U., Ramadoss, A., Ede, S. R. & Kundu, S. DNA mediated wire-like clusters of self-assembled TiO<sub>2</sub> nanomaterials: supercapacitor and dye sensitized solar cell applications, *Nanoscale* **6**(14), 8010–8023, <https://doi.org/10.1039/C4NR01836B> (2014).
49. Ramimoghdam, D., Bagheri, S. & Abd Hamid, S. B. Biotemplated synthesis of anatase titanium dioxide nanoparticles via lignocellulosic waste material, *BioMed Res. Int.* **2014**. <https://doi.org/10.1155/2014/205636> (2014).
50. Caratão, B., Carneiro, E., Sá, P., Almeida, B. & Carvalho, S. Properties of electrospun TiO<sub>2</sub> nanofibers, *J. Nanotechnol.* **2014**. <https://doi.org/10.1155/2014/472132> (2014).
51. Gao, R., Huang, Y., Liu, D. & Li, G. Effect of heat treatment process on the structure and properties of nano-TiO<sub>2</sub>. *Nat. Environ. Pollution Technol.* **20**(1), 405–410. <https://doi.org/10.46488/NEPT.2021.v20i01.048> (2021).
52. Wang, L. et al. Preparation, characterization, and photocatalytic activity of TiO<sub>2</sub>/ZnO nanocomposites, *J. Nanomater.* 15–15. <https://doi.org/10.1155/2013/321459> (2013).
53. Behzadi, S. et al. Cellular uptake of nanoparticles: journey inside the cell. *Chem. Soc. Rev.* **46**(14), 4218–4244. <https://doi.org/10.1039/C6CS00636A> (2017).
54. Colapicchioni, V. et al. Personalized liposome–protein corona in the blood of breast, gastric and pancreatic cancer patients. *Int. J. Biochem. Cell Biol.* **75**, 180–187. <https://doi.org/10.1016/j.biocel.2015.09.002> (2016).

### Author contributions

M.A. and M.J.A did Conceptualization and M. I.A, R.A.G, M.A, and M.J.A did methodology, and R.A.G and M.A applied software, and M.J.A, R.A.G, and M.A investigated validation and M.I.A did formal analysis, M. I.A, R.A.G, M.A., and M.J.A did the investigation, M.A and R.A.G did data curation, M.I.A, R.A.G, M.A, and M.J.A wrote the manuscript, M.A, R.A.G, and M.J.A did the review and editing, and M.A. is the supervision of the project and R.A.G, M.J.A, and M.A are project administration. All authors have read and agreed to the published version of the manuscript. Also, all authors reviewed the manuscript.

### Funding

This research did not receive any specific grant from funding agencies.

### Declarations

### Competing interests

The authors declare no competing interests.

### Ethical approval

It is not applicable because the studies were done in vitro.

### Additional information

**Correspondence** and requests for materials should be addressed to M.A.

**Reprints and permissions information** is available at [www.nature.com/reprints](http://www.nature.com/reprints).

**Publisher's note** Springer Nature remains neutral with regard to jurisdictional claims in published maps and institutional affiliations.

**Open Access** This article is licensed under a Creative Commons Attribution-NonCommercial-NoDerivatives 4.0 International License, which permits any non-commercial use, sharing, distribution and reproduction in any medium or format, as long as you give appropriate credit to the original author(s) and the source, provide a link to the Creative Commons licence, and indicate if you modified the licensed material. You do not have permission under this licence to share adapted material derived from this article or parts of it. The images or other third party material in this article are included in the article's Creative Commons licence, unless indicated otherwise in a credit line to the material. If material is not included in the article's Creative Commons licence and your intended use is not permitted by statutory regulation or exceeds the permitted use, you will need to obtain permission directly from the copyright holder. To view a copy of this licence, visit <http://creativecommons.org/licenses/by-nc-nd/4.0/>.

© The Author(s) 2024